nature communications

Article

https://doi.org/10.1038/s41467-024-54799-6

Nanoscale polarization transient gratings

Received: 8 May 2024

Accepted: 21 November 2024

Published online: 30 December 2024

Check for updates

Laura Foglia[1] ✉, Björn Wehinger[1,2,10], Giovanni Perosa[1,3], Riccardo Mincigrucci[1], Enrico Allaria[1], Francesco Armillotta[3], Alexander Brynes[1], Matthew Copus[4], Riccardo Cucini[5], Dario De Angelis[1], Giovanni De Ninno[1,6], W. Dieter Engel[7], Danny Fainozzi[1,11], Luca Giannessi[1,8], Ezio Iacocca[4], Nupur N. Khatu[1,2,9], Simone Laterza[1,3], Ettore Paltanin[1,3], Jacopo Stefano Pelli-Cresi[1], Giuseppe Penco[1], Denny Puntel[3], Primož Rebernik Ribič[1], Filippo Sottocorona[1,3], Mauro Trovò[1], Clemens von Korff Schmising[7], Kelvin Yao[7], Claudio Masciovecchio[1], Stefano Bonetti[2] & Filippo Bencivenga[1]

Light manipulation at the nanoscale is essential both for fundamental science and modern technology. The quest to shorter lengthscales, however, requires the use of light wavelengths beyond the visible. In particular, in the extreme ultraviolet regime these manipulation capabilities are hampered by the lack of efficient optics, especially for polarization control. Here, we present a method to create periodic, polarization modulations at the nanoscale using a tailored configuration of the FERMI free electron laser and demonstrate its capabilities by comparing the dynamics induced by this polarization transient grating with those driven by a conventional intensity grating on a thin ferrimagnetic alloy. While the intensity grating signal is dominated by the thermoelastic response, the polarization grating excitation minimizes it, uncovering helicity-dependent responses previously undetected. We anticipate nanoscale polarization transient gratings to become useful for the study of physical, chemical and biological systems possessing chiral symmetry.

Manipulating light at the nanoscale is a major challenge for modern science, with the potential to unveil fundamental aspects of light–matter interactions and to enable advances in key technologies such as light harvesting, imaging, biosensing, or catalysis. In the visible range, nanoscale control of radiation properties such as intensity and phase is often achieved via artificial structures with dimensions comparable to or shorter than the wavelength, such as metasurfaces, photonic crystals, and plasmonic nanostructures[1–3]. Instead, nanoscale control of light polarization remains particularly challenging. Spatially variable inhomogeneous vector beams can be generated, for instance, by using specially designed metasurfaces[4], but a straightforward approach at short wavelengths, i.e. in the extreme ultraviolet and X-ray regime, is yet to be found.

The use of EUV and X-ray radiation in a transient grating (TG) scheme provides an alternative way to control electromagnetic fields at the nanoscale. In fact, the brightness of EUV free electron laser (FEL) pulses allows to efficiently generate sinusoidal patterns of light intensity with spatial periodicity in the 10–100 nm range[5,6], without

[1]Elettra - Sincrotrone Trieste S.C.p.A., S.S. 14 km 163.5 in Area Science Park, 34149 Trieste, Italy. [2]Department of Molecular Sciences and Nanosystems, Ca' Foscari University of Venice, 30172 Venezia, Italy. [3]Department of Physics, Universitá degli Studi di Trieste, 34127 Trieste, Italy. [4]University of Colorado Colorado Springs, Center for Magnetism and Magnetic Nanostructures, Colorado Springs, CO 80918, USA. [5]CNR- Istituto Officina dei Materiali (IOM), Unità di Trieste, Strada Statale 14, km 163.5, 34192 Basovizza, TS, Italy. [6]Laboratory of Quantum Optics, University of Nova Gorica, 5270 Ajdovščina, Slovenia. [7]Max-Born-Institute for Nonlinear Optics and Short Pulse Spectroscopy, 12489 Berlin, Germany. [8]INFN Laboratori Nazionali di Frascati, Via E. Fermi 54, 00044 Frascati Roma, Italy. [9]European XFEL, Holzkoppel 4, 22869 Schenefeld, Germany. [10]Present address: European Synchrotron Radiation Facility, 71 Avenue des Martyrs, Grenoble 38000, France. [11]Present address: Institute of Applied Physics, University of Bern, Sidlerstrasse 5, Bern 3012, Switzerland.
✉e-mail: laura.foglia@elettra.eu

https://doi.org/10.1038/s41467-024-54799-6

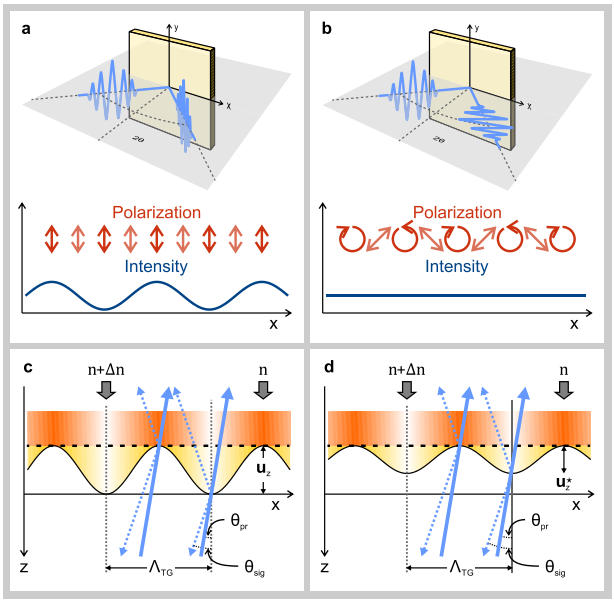

Fig. 1 | Intensity vs polarization grating excitation. a PP beams generate an intensity grating with period Λ_{TG} and constant polarization. **b** OP beams generate a modulated polarization with the same periodicity and constant intensity. **c** Diffraction from an intensity TG resulting from surface modulations $\mathbf{u}_z$ and refractive index variations. The first typically dominates the backward-diffracted signal and the latter the forward diffraction. **d** Diffraction from a polarization TG, where the thermal modulation depends on the dichroic absorption $\Delta\beta$, reducing $\mathbf{u}_z^\star$. The signal can still originate from refractive index variations associated with the chiral dispersion $\Delta\delta$.

requiring any physical modification of the sample. This EUV TG excitation is then capable of driving ultrafast nanoscale dynamics in a controlled way, and it has recently proven to be an effective tool for investigating the thermal and mechanical properties of matter in a length-scale range previously inaccessible[7,8]. Additionally, the access to core resonances provides unprecedented insights into the electronic and magnetic dynamics at such a lengthscale[9,10].

In a TG experiment, two pulses of the same wavelength λ_{ex} and intensity I_0, overlapped in time and space and at a given crossing angle 2θ at the sample, generate a transient interference pattern along the transverse plane (x, y), as defined in Fig. 1a and b. If the two excitation beams are parallel-polarized (PP), as in panel **a**, the intensity at the sample is fully modulated and given by $I_{ex} = 2I_0(1+\cos qx)$, where **q** is the TG wavevector. The spatial periodicity is given by $\Lambda_{TG} = \lambda_{ex}/2\sin(\theta) = 2\pi/q$, while the polarization remains uniform. Instead, when the two beams are orthogonal-polarized (OP), the polarization is modulated with the same periodicity Λ_{TG}, ranging from circular left to circular right, while the intensity remains uniform[11–14], as depicted in Fig. 1b. Therefore, EUV polarization TGs enable the generation of spatial modulations of light polarization with values of Λ_{TG} comparable to those of $\lambda_{ex} \approx 10$–100 nm.

If the periodic excitation modulates the EUV complex refractive index $n = 1-\delta+i\beta$ at the wavelength of the probe λ_{pr}, both intensity and polarization gratings can be revealed by the diffraction at an angle θ_{sig} of an EUV probe beam incident at the angle θ_{pr}, as shown in Fig. 1b and c. The diffraction intensity as a function of the arrival time difference Δt between the probe and the TG excitation encodes information on the sample dynamics. Typically, the interaction of matter with an intensity TG excitation in the EUV range is dominated by absorption and after ≈100 fs, the periodically photoexcited electrons transfer their energy to the lattice via electron-phonon coupling, leading to a temperature grating[7]. The formation of the temperature modulation is usually followed by a thermal time- and space-dependent density modulation $\Delta\rho(x, \Delta t)$ between the excited and unexcited areas. Similarly, magnetic samples sustain a periodic ultrafast demagnetization $\Delta\mathbf{M}(x, \Delta t)$[9] in correspondence to the hot photoexcited areas. Both these thermal effects induce the periodic variation of the refractive index $\Delta n(x, \Delta t)$ that is required for diffraction to occur. We note that the density modulation is visible at any λ_{pr}, since $(\delta, \beta) \propto \rho$, whereas λ_{pr} needs to be resonant with a dichroic absorption edge in order to observe the effects of the magnetization[9,10]. Note that the figure neglects the ultrafast, sub-ps, electronic contribution to Δn since the whole discussion concentrates on the ps dynamics.

Additionally, an intensity grating is associated with a surface displacement, $\mathbf{u}_z(x, \Delta t) = \mathbf{u}_z(\Delta t)(1+\cos qx)/2$ (see the yellow area in Fig. 1c), also resulting from thermal expansion, which leads to diffraction of the probe via interference of photons with different path lengths. In backward diffraction, the contribution of surface displacement typically dominates and vanishes only in the absence of a temperature grating, while the effects of Δn are accessed via the modulation in the EUV reflectivity[7,8].

The response to an EUV polarization TG depends on the dichroic correction to the refractive index $n^{\pm} = (1-\delta \pm \Delta\delta) + i(\beta \pm \Delta\beta)$ at the excitation wavelength, where the sign + (−) refers to circular right (left) light. Since the excitation intensity is uniform, the temperature modulation depends only on the dichroic absorption $\Delta\beta$ and thereby also the magnitude of surface displacement $\mathbf{u}_z^\star(x, \Delta t)$, bulk density modulations $\Delta\rho^\star(x, \Delta t)$ or thermally-driven ultrafast demagnetization, which could even be fully suppressed for $\Delta\beta = 0$, i.e. in the absence of dichroic absorption. This is exemplarily schematized by a smaller yellow area in Fig. 1d. Nevertheless, the polarization grating can still modulate the refractive index, provided that the sample shows a chiral response in its real part $\Delta\delta$. In other words, a polarization grating can be used to reduce or suppress thermal contributions to $\Delta n(x, \Delta t)$ and to enhance, or isolate, other helicity-dependent light-matter couplings.

In this work, we demonstrate the potential of polarization transient gratings by comparing the dynamics induced on a ferrimagnetic alloy with those driven by the conventional intensity grating excitation. Indeed, while the intensity TG signal is dominated by the thermoelastic response of the sample, polarization TG excitation minimizes it, uncovering helicity-dependent dynamics previously hidden. This unique capability can be broadly applied to reveal helicity-dependent dynamics at the nanoscale and with ultrafast time resolution in any system possessing chiral symmetry.

Results

Practically, however, realizing EUV polarization gratings is not a trivial endeavor. Indeed, efficient generation and probing of EUV TGs requires crossing three FEL beams at a finite angle at the sample, one of which needs to be variably delayed. As discussed in detail elsewhere[8,15], the highest TG efficiency through the whole EUV spectrum is ensured by using exclusively reflective optics while minimizing the intensity ratio between the two pump beams. This idea is at the basis of the TIMER instrument at the FERMI FEL (Trieste, Italy), which was used in this experiment and is shown in Fig. 2a. The probe beam is split from the FEL output geometrically by reflecting vertically off a planar mirror (PM1) before entering the mulilayer-based delay line[16]. Similarly, the two pump beams are usually split horizontally with a second planar mirror (PM2), the reflectivity of which controls the intensity balance between the pump beams and, thus, the TG contrast. In this context, the excitation of a polarization grating requires independently controlling the polarization of each excitation pulse. Polarization control after the EUV source has been demonstrated using phase retardation upon reflection off metallic mirrors[17] with the generation of circular-polarized beams from a linear-polarized source. An analogous approach could, in principle, be used to transform from circular to linear polarization. Thus, by placing such a mirror-based system along

https://doi.org/10.1038/s41467-024-54799-6

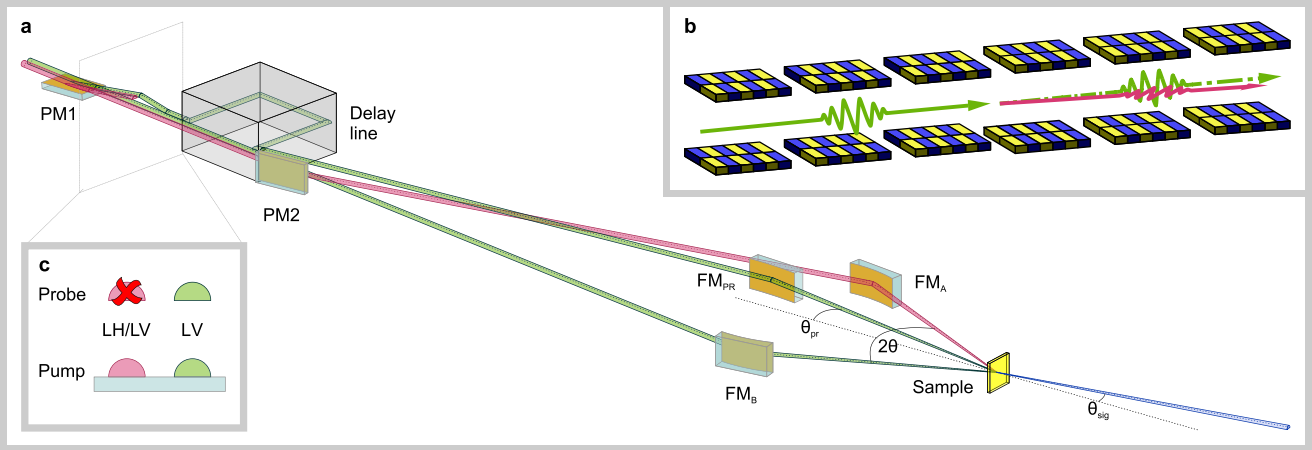

Fig. 2 | Experimental setup. a Scheme of the TIMER instrument in the OP beam configuration. The two beams generated by the FEL source are split vertically by a planar mirror PM1 to generate the probe (see panel **c**). Of the remaining two half beams, the variably polarized one (LH/LV) is steered by the second planar mirror PM2 whereas the LV branch propagates unaffected. Both half beams constitute the pump and are crossed and focussed at the sample at an angle 2θ by two toroidal mirrors FM1 and FM2. Of the two half beams reflected by PM1, the variably polarized one is geometrically blocked while the LV is steered to the delay line and then focussed at the sample at an angle θ_{pr}. The signal beam is drawn exemplary to propagate in forward diffraction at an angle θ_{sig}. **b** Scheme of the OP beam generation in the FERMI undulator chain (see text for discussion).

each of the two pump beams and allowing one of these two systems to rotate by 90° around the beam axis, one could generate both intensity and polarization TGs starting from a circularly polarized pulse at the FEL output. However, the degree of polarization and the overall throughput of the system proposed in ref. 17, which vary strongly with the wavelength, are limited respectively to 90% maximum and about 20% at the corresponding wavelength. This would result in an overall decrease of the signal by almost two orders of magnitude and, more importantly, a strong contamination of the signal by an intensity TG background due to the low polarization contrast. Alternative schemes based on multilayer mirrors working at the Brewster angle could improve the polarization contrast, albeit largely narrowing the instrument bandwidth and, therefore preventing spectroscopic approaches based on OP beams. On the other hand, beam polarization can be controlled at the EUV source[18–26] but, to date, this did not allow the simultaneous generation of multiple EUV pulses with different polarization and direction. Instead, here we present a special configuration of the FERMI FEL, based on a split-undulator scheme that permits to, simultaneously obtain a pair of EUV pulses with independent linear polarization emitted along slightly different horizontal directions. In standard FEL operation, the trajectory of the electron beam in the undulator chain, consisting of six APPLE-II[27] radiators, is kept straight using dipole magnets. Here, the undulator chain of FERMI FEL-1[28] is divided into two sections of three radiators each, and the dipole magnets are used to steer the electron beam initially along a slightly off-axis trajectory through the first section. Then, at the center of the undulator chain, the beam is strongly kicked and steered along a symmetrical off-axis trajectory through the second section[29], as schematically depicted in Fig. 2b. The first section is used to generate linear vertical (LV) light while the emission of the second one is tuned either to parallel (LV) or orthogonal (linear horizontal - LH) polarization[30]. This allows to switch from PP to OP beams without changing any other experimental parameter. Moreover, the symmetry with respect to the undulator axis ensures that the two beams have a balanced relative pulse energy, even partially compensating for the reflectivity of PM2. In this scheme, PM2 is not used to split the pump beams as usual, but only to deflect one of the two along its trajectory. Differently from the common TIMER configuration, there are thus two separate beams coming from the FEL source, which are both split vertically to generate the probe (see Fig. 2c). Since the delay line transmits only LV polarized light, the half-beam along the probe path that changes polarization is blocked, to ensure that the probe intensity at the sample remains constant in both the OP and PP beams configuration. In this split-undulator scheme the FEL throughput is about 20% of the standard configuration, thus with a similar efficiency to an eventual mirror-based setup for controlling the polarization after the FEL source. Nevertheless, the scheme retains the flexibility of the standard configuration both in terms of wavelength tunability range and full polarization control, including states in the Poincaré sphere that cannot be achieved with mirrors, such as elliptical polarization. Further details on the accelerator setup are provided in Section 1 of the Supplementary Information.

To demonstrate experimentally the generation of a polarization TG with a $\Lambda_{TG} = 43.6$ nm period ($2\theta = 27.6°$), the FEL is tuned at an operating wavelength of 20.8 nm to probe resonantly and in backward diffraction at the Co M-edge in a ferrimagnetic CoGd alloy thin film. At the same resonant energy but in forward diffraction, Ksenzov et al.[9] have previously observed a strong TG signal in this material. The intensity of this signal, for Δt larger than hundreds of fs, is mainly determined by the thermal magnetization modulation $\Delta\mathbf{M}(x, \Delta t) \propto \Delta\mathbf{M}(\Delta t)(1 + \cos qx)/2$. The signal depends linearly on the induced temperature difference and exhibits a clear non-sinusoidal time-dependence with a few ps rise and sub-100 ps decay time, reproduced also in other magnetic compounds using polarization analysis of the signal[10]. Furthermore, TG signal decay strongly depends on Λ_{TG}, indicating lateral thermal transport (i.e. along the grating wavevector) as responsible for the signal decay. In backward diffraction, the magnetization modulation at the film surface could lead to a modulation of the EUV reflectivity and thus to a signal of a magnetic nature, but the $\mathbf{u}_z(x, \Delta t)$ contribution is expected to be dominant, according to previous results[31] and considering the usually large thermal expansion coefficients of metallic films. The exact temporal evolution of the surface-induced signal is generally unknown a priori. Nevertheless, in these nm-thick layered samples on a bulk substrate the response typically consist of a combination of surface acoustic waves (SAW), Lamb modes, and leaky waves that are all associated with sinusoidal waveforms in time. Thus, the sinusoidal thermoelastic and the non-sinusoidal magnetic dynamics can be easily discerned on the ps timescale.

Figure 3a depicts the backward-diffracted intensity TG signal (PP pump beams) as blue circles, clearly showing the ultrafast electronic response at time zero, followed by the sinusoidal oscillatory waveform

https://doi.org/10.1038/s41467-024-54799-6

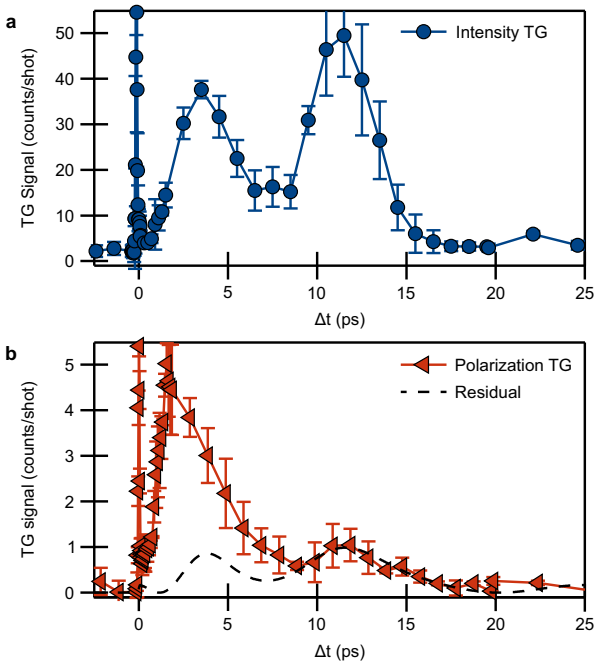

Fig. 3 | Dynamics induced by intensity vs polarization grating excitation. **a** Intensity grating. Blue circles: backward-diffracted TG signal from PP beams. **b** Polarization grating. Red triangles: backward-diffracted signal from OP beams. Dashed line: residual sinusoidal component (see text for discussion). Error bars in **a** and **b** are the variance calculated over three scans. Center value is the mean.

typical of the thermoelastic response. The long-time dynamics are plotted for reference in Section 2 of the Supplementary Information. Fitting with a sum of cosinusoidal terms results in two dominating phonon modes. Their frequencies ($\nu_S \approx 43$ GHz and $\nu_{LA} \approx 123.0$ GHz) are compatible with the expected frequencies of the SAW and longitudinal acoustic (LA) phonon, respectively. A more detailed discussion of the ultrafast electronic response, the thermoelastic properties of the sample, and the fitting procedure are given in Section 2 of the Supplementary Information.

We compare this signal with the one obtained with OP pump beams, plotted as red triangles in Fig. 3b. After the time-zero spike, the two dynamics strongly differ up to 10 ps, where the latter signal is dominated by a clear non-sinusoidal time-dependence with a 2 ps rise and a sub-10 ps decay. On a longer timescale oscillatory dynamics are observed at the same frequencies, suggesting the presence of a weak residual modulation of surface displacement. Indeed, from ≈10 ps on, the dynamics can be reproduced by scaling the fit to the signal from the intensity grating, as indicated by the dashed line in Fig. 3b. Within the assumption that the non-sinusoidal signal is of dichroic nature, and therefore has orthogonal polarization with respect to the oscillatory component, the two signal intensities add up incoherently (without interference term), and the resulting scaling factor is $\alpha = 0.019$. Nevertheless, even without this assumption, the fit results are not changing significantly (see Supplementary Information Section 2).

Discussion

This residual intensity contrast can have a two-fold origin: (i) a non-perfect orthogonal polarization of the two FEL pulses, discussed in Section 1 of the Supplementary information, and (ii) a remaining temperature grating due to dichroic absorption $\Delta\beta$, as discussed previously. As an order of magnitude estimate of the second mechanism, we write the amplitude of the fully modulated thermal grating resulting from intensity TG excitation with incident intensity $2I_{0,PP}$ as $\Delta T \propto 4I_{0,PP}/L_{abs}\sigma_{ex}^2$, where σ_{ex} and $L_{abs} = \lambda_{ex}/4\pi\beta$ are the FEL spot size and the average absorption length, respectively. In the case of the polarization grating, for an incident intensity $2I_{0,OP}$ the residual temperature grating has an amplitude $\Delta T^\star \propto (2I_{0,OP}/\sigma_{ex}^2)(1/L_{abs}^- - 1/L_{abs}^+)$ around the average temperature $T^\star \propto 2I_{0,OP}/L_{abs}\sigma_{ex}^2$. Here $L_{abs}^\pm = \lambda_{ex}/4\pi(\beta \pm \Delta\beta)$ account for the different absorption lengths for left and right circular polarization. The two temperature modulations are schematically depicted in Fig. 4a. Since (A) the spot size and overlap conditions are the same for intensity and polarization gratings, (B) the amplitude of the surface modulations $\mathbf{u}_z$ and $\mathbf{u}_z^\star$ are linearly proportional to the temperature modulation and (C) the TG signal is proportional to $\mathbf{u}_z^2(x,\Delta t)$, the ratio between the sinusoidal thermoelastic signal in intensity and polarization TGs can be written as $(\Delta T^\star/\Delta T)^2 \times \zeta = (I_{0,OP}/I_{0,PP})^2(\Delta\beta/\beta)^2 \times \zeta \approx 0.007$, where $\zeta \approx 11/9$ is the ratio between the probe intensities in the two measurements. The estimation of the absorption coefficients β and $\Delta\beta$ is provided in the Methods section. The calculated value is on the same order of magnitude as the scaling factor α extracted from the data analysis but smaller than expected, given the additional contribution from the FEL polarization unbalances to the TG contrast (mechanism (i)).

Instead, the significant change in the time-dependence of the TG signal when changing from PP to OP beams is a clear indication of the generation of a polarization transient grating. Indeed, such a strong difference in the picosecond dynamics reveals the relative enhancement of a signal component that cannot be attributed to the thermoelastic response.

In the case of a polarization TG, any mechanism related to a temperature contrast $\Delta T^\star$ after a sub-ps thermalization can instead be ruled out. As sketched in Fig. 4b for the example of magnetization and density, the temperature variation ΔT due to the intensity TG drives both a magnetization change $\Delta\mathbf{M}$ and a density change $\Delta\rho$, with an associated surface displacement $\mathbf{u}_z$. Similarly, a temperature variation $\Delta T^\star$ due to the polarization TG would induce a magnetization change $\Delta\mathbf{M}^\star$, a density change $\Delta\rho^\star$ and a surface displacement $\mathbf{u}_z^\star$. For small temperature variations, all these modulations can be approximated to depend linearly on the temperature. Hence, all the thermally-driven signal components should scale comparably when changing from intensity to polarization TG and one could expect to observe the whole signal to scale with the much smaller induced $\Delta T^\star$, without any change in its time-dependence. However, we do not observe such behavior. Rather, the emergent ps-dynamics in the polarization TG signal must be associated with a non-thermal, i.e. without changes in the electronic and lattice temperature, modulation of the complex refractive index driven by the direct interaction of matter with the periodic modulation of the light polarization. In a ferrimagnet this helicity-dependent response is most probably of magnetic nature.

To test whether a direct modulation of the magnetic system can result in the observed qualitative signal, we performed numerical simulations. We use a pseudospectral model that includes both short and long-range exchange interactions and has been recently shown to agree with atomistic spin dynamics after the electronic-induced magnetization distribution has been established[32]. The 2D simulation disregards thermoelastic responses and, consequently, any magnetoelastic coupling. The magnetization evolves solely due to exchange, anisotropy, and damping. Under the assumption that the polarization TG induces a non-thermal change in the magnetization, we model our initial condition as a deterministic polarization TG component on a stochastic thermally-driven uniform demagnetization. This initial condition is assumed to be established after a time t_0, i.e., after the ultrafast excitation mechanism has fully developed[33]. The details regarding the implementation and initial conditions are discussed in the Methods and in Section 3 of the supplementary information.

We performed simulations with several exchange lengths L_{ex}, chosen to qualitatively describe the experimental signal while being physically plausible for a CoGd alloy. The time dependence of the

https://doi.org/10.1038/s41467-024-54799-6

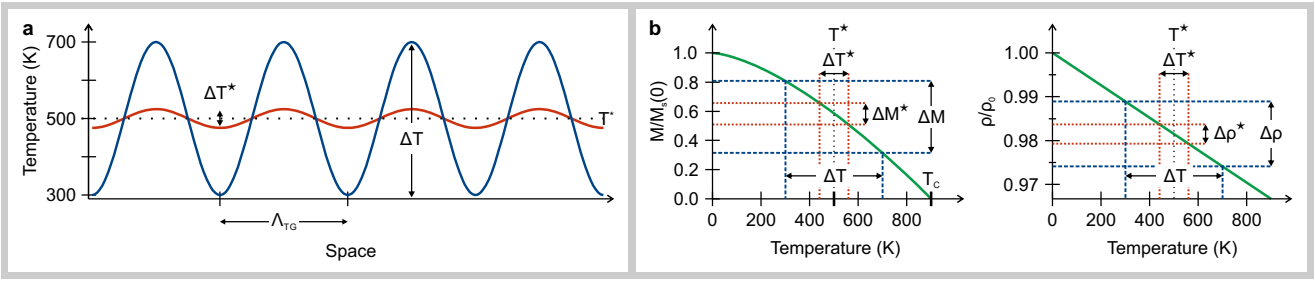

Fig. 4 | Modulation of sample parameters induced by intensity vs polarization grating excitation. a Temperature gradient ΔT (blue curve) induced by intensity TG compared with the residual temperature modulation ΔT^* (red curve) around T^* (dotted line) associated with dichroic absorption in polarization TG. **b** Changes in magnetization $\Delta\mathbf{M}$ and density $\Delta\rho$ driven by the temperature modulation ΔT and the corresponding $\Delta\mathbf{M}^*$ and $\Delta\rho^*$ due to ΔT^*. Please note that here $\Delta\mathbf{M}^*$, $\Delta\rho^*$ and ΔT^* are multiplied by a factor 5 to be visible on the scale.

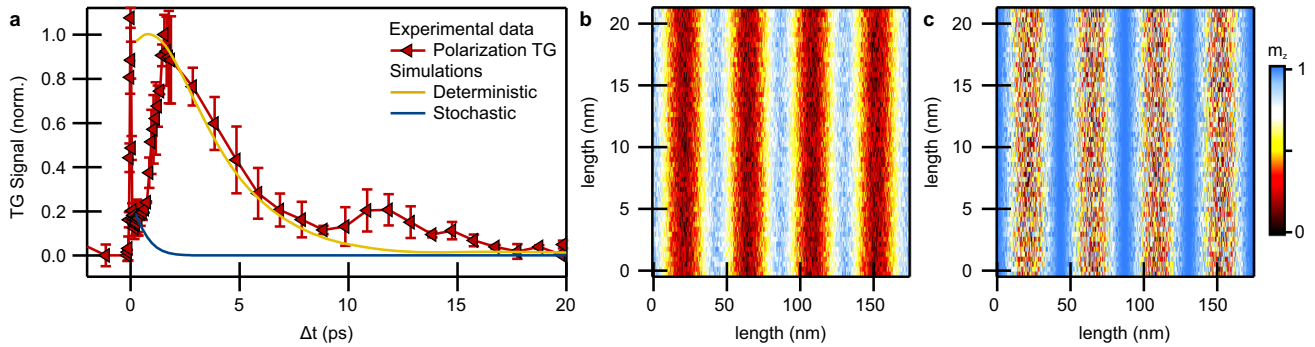

Fig. 5 | Dynamics induced by stochastic vs deterministic magnetic modulations. a Experimental data (red line with markers) vs. calculations for deterministic (yellow) and stochastic (blue) initial conditions. See text for discussion. Center value and error bars are, respectively, mean and variance of the data. **b** and **c** Two-dimensional plots of the initial conditions in the deterministic (polarization TG) and stochastic (intensity TG) simulations, respectively. The color scale is the same for both plots.

estimated signal from the polarization TG simulations at $L_{ex} = 4$ nm (see the "Methods" section) is shown in Fig. 5a by a yellow line. The experimental signal is shown in comparison by red symbols. The simulation results have been normalized to match the experimental signal peak and begin at a delay of $t_0 = 250$ fs to account for the simulations being initialized after the electronic-induced demagnetization. This choice of delay is representative of ultrafast optical quench of metals, as discussed in Section 3 of the Supplementary Information, and, most importantly, does not substantially affect the comparison proposed in Fig. 5a. The simulations exhibit an increase in the signal in qualitative agreement with the experiments. This maximum peak subsequently decays in good quantitative agreement between simulations and experiments. Instead, as evidenced by the blue trace, initial conditions describing a non-deterministic but thermal (stochastic) modulation at the same demagnetization change $\overline{M_T}$ do not qualitatively reproduce the data. The two simulation cases are scaled by the same factor to maintain the relative intensity differences. Despite its simplicity, the model is thus capable of reproducing the observed ps dynamics, indicating that it originates from a non-thermal magnetic contribution.

The understanding of the underlying excitation mechanism at the origin of the polarization TG signal goes beyond the scope of the current demonstrative experiment and would require a three dimensional extension of the theory to take into account also the elastic and magneto-elastic response. Nevertheless, irrespective of any specific excitation mechanisms, the qualitative comparison between calculations and experimental data suggests a magnetic origin of the signal, likely arising from a direct helicity-dependent coupling that adds on top of a spatially uniform (thermally-driven) demagnetization background. For example, recent experiments have shown the inverse Faraday effect (IFE) to be unexpectedly strong at these excitation wavelengths[34]. These results already reveal how the comparison of intensity and polarization TG studies could provide relevant insights into the intricate physics of chiral systems. This holds particularly in the EUV and soft X-ray regimes, where one could exploit the strong variation of dichroic absorption $\Delta\beta$ around resonances. Indeed, a small photon-energy change would allow for a strong effect on the relative weight of dichroic absorption ($\Delta\beta$) and dispersion ($\Delta\delta$) in the changes induced to the refractive index by the periodic pattern of circular left and circular right polarization light. Additionally, investigating the dependence of the signal on the polarization TG period could allow to explore the role of the exchange interaction and spin transport at their characteristic lengthscales and in the absence of lateral thermal transport. Furthermore, the dependence on Λ_{TG} could be affected by lateral domain size, when the two become commensurate, thus potentially allowing the investigation of the role of domain size and their walls' dynamics in ultrafast demagnetization phenomena.

In conclusion, we applied a tailored FEL setting and the TG instrument available at FERMI to demonstrate the generation of an ultrafast polarization grating with a 43.6 nm period, by selectively reducing the thermoelastic response of a magnetic system while enhancing a previously hidden signal component. Our approach is not limited to magnetic systems but can be extended to all systems that have a chiral response. Moreover, the use of EUV pulses provides both access to the nanoscale and a playground to tune circular absorption and dispersion coefficients with respect to each other and, thereby, the relative weight of thermal and helicity-dependent excitation. In this context, we anticipate that polarization TG experiments could be applied to investigate chiral opto-magnetic properties and the valley degree of freedom of emerging topological systems where the

characteristic lengthscales are on the order of the EUV TG periodicities, such as metal dichalchogenides[35], twisted bilayer graphene[36] or Weyl semimetals[37]. Indeed, such an excitation scheme has been proposed theoretically for the unambiguous identification of dynamical axions in this class of condensed matter systems[38].

Methods

Sample and experimental parameters

The sample was a 15 nm-thick film of $Co_{0.78}Gd_{0.22}$ alloy with perpendicular magnetic anisotropy, analogous to the one used in reference[9]. The magnetic stack consisting of (1.5 nm Ta/1.5 nm Pt/15 nm $Co_{0.78}Gd_{0.22}$/3 nm Pt) was grown on a lead-germanate glass substrate using dc- and rf-magnetron sputtering at room temperature (base pressure of 3×10^{-8} mbar). Ar is used as a sputter gas at a pressure of 3.4×10^{-3} mbar. Typical deposition rates range between 0.1 and 0.4 As^{-1}. The CoGd layer exhibits an out-of-plane anisotropy with a coercive field of approximately 70 mT and was magnetized to saturation with the magnetic field normal to the film surface. The compensation temperature is above room temperature, which is why the magnetization is dominated by Gd. Similar to other work we expect a Curie temperature larger than 600 K[39] and around 900 K[40]. The absorption coefficients used for the estimation of the residual temperature modulation observed in Fig. 3b of the main text are $|\beta| = 0.1$[41] and $\Delta\beta = -6.12\times10^{-3}$. The latter was calculated assuming that the magneto-optical constants at the Co M-edge are determined by the number of Co atoms per unit volume and using $\Delta\beta_{Co} = -1.1\times10^{-2}$ as the dichroic absorption of pure Co[42].

The excitation fluence at the sample was about 2 mJ/cm^2, the 2 nm Ta capping layer transmits 89% of the incident light and we calculate a penetration depth of 16.5 nm in the ferrimagnetic layer. We estimate a local lattice heating due to FEL excitation of about 400 K. Each acquisition was integrated over 1500 shots per delay point with a FEL repetition rate of 50 Hz and a pulse duration of ≈40 fs. We measured the total diffracted signal without polarization analysis.

Numerical modeling

The pseudospectral Landau–Lifshitz model simulates the Landau–Lifshitz equation

$$\frac{\partial}{\partial t}\mathbf{m} = -\mathbf{m}\times\mathbf{\Omega}_{\text{eff}} - \alpha_G\mathbf{m}\times\left(\mathbf{m}\times\mathbf{\Omega}_{\text{eff}}\right), \tag{1}$$

where $\mathbf{m}$ is the normalized magnetization vector, $\mathbf{\Omega}_{\text{eff}}$ is an effective field contribution expressed in units of rad/s containing the relevant physics of the system, and α_G is the dimensionless Gilbert damping coefficient. In this case, we consider the effect of an externally applied field contribution $\gamma\mu_0\mathbf{H}_0$, where γ is the gyromagnetic ratio, μ_0 is the vacuum permeability, and $\mathbf{H}_0$ is the uniform external field; and the exchange contribution $\mathcal{F}^{-1}\{\omega(k)\hat{\mathbf{m}}\}$, where $\mathcal{F}^{-1}\{\cdot\}$ represents the inverse Fourier transform, $\hat{\mathbf{m}}$ is the Fourier transform of the magnetization components, and $\omega(k)$ is the magnon dispersion relation. The pseudospectral model is applicable to situations where both short and long wavevectors are relevant to the dynamics since the system's energy and momentum relation is encoded in the dispersion relation. In other words, this model describes the spatiotemporal range between atomistic spin dynamics and micromagentic simulations. For a 2D magnetic surface, we implement the pseudospectral model with the dispersion relation[43]

$$\omega(k) = \gamma\mu_0 M_s 2\left(\frac{L_{ex}}{a}\right)^2\left(2-\cos(k_x a)-\cos(k_y a)\right) \tag{2}$$

where M_s is the saturation magnetization, L_{ex} is the ferromagnetic exchange length, a is the lattice constant, and $\mathbf{k} = (k_x, k_y)$ is the wavevector. In this model, we do not account for the dynamic coupling to the phonon system and it is applicable to CoGd in its low-energy sector. We also disregard the effect of non-local dipole fields since these have been shown to be negligible in ultrafast conditions[44]. Finally, we note that the exchange length is difficult to predict for an alloy in far-from-equilibrium conditions. We estimated the exchange length to lie in the range between Co and Gd. A weighted average based on composition suggests $L_{ex} = 12$ nm, however, we expect a shorter exchange length at far-from-equilibrium conditions. As shown in the main text, $L_{ex} = 4$ nm returns qualitatively similar behavior between simulations and experiments.

The initial magnetization distribution for polarization TG is defined after a time t_0, i.e., after the ultrafast pump establishes said distribution, and the model does not rely on any specific mechanism for bringing the system to the initial out-of-equilibrium conditions. We thus consider the following functional form for the initial state:

$$m_z^{(PG)}(x,y,t=t_0) = 1-\xi(x,y)\frac{\overline{\Delta M}_T}{M_s}\left[\frac{1}{2}-\alpha\cos(qx)\right] - C\frac{1-\cos(qx)}{2} \tag{3}$$

where $\overline{\Delta M}_T$ is the maximum magnetization quench induced thermally, $C = \frac{\overline{\Delta M}_{PG}}{M_s} \le 1-\frac{\overline{\Delta M}_T}{M_s}(\frac{1}{2}+\alpha)$ is a coefficient that determines the strength of the modulation due to the light polarization grating, $\alpha = \Delta\beta/\beta = 0.06$ is the amplitude of the residual intensity grating due to dichroic absorption, $\mathbf{q}$ is the grating wavevector, and $\xi(x, y)$ is a uniformly distributed random noise in space defined in the range [0,1]. The in-plane magnetization distributions are defined as $m_x^{(PG)}(x,y,t=t_0) = \sqrt{1-[m_z^{(PG)}(x,y,t=t_0)]^2}\cos(\eta(x,y))$ and $m_y^{(PG)}(x,y,t=t_0) = \sqrt{1-[m_z^{(PG)}(x,y,t=t_0)]^2}\sin(\eta(x,y))$ where η is a uniformly distributed random number in the range $[0, 2\pi]$. Cast in spherical coordinates, we see that $\xi(x,y) = \cos(\theta)$, where θ is the polar angle, and $\eta(x, y)$ is the azimuth. Therefore, we generate a Gaussian noise in the unit sphere, similar to the Box–Muller algorithm[45]. This strategy ensures that the magnetization vector maintains a constant magnitude, as expected from the modeled quasi-equilibrium conditions, and that its distribution obeys the fluctuation-dissipation theorem[46]. Such a random magnetization distribution has been shown to be a good descriptor of a thermal demagnetization insofar as the electronic bath is in equilibrium[47], which is typically the case after about 250 fs for metallic alloys. Examples of initial conditions and the resulting time evolution are shown in Section 3 of the Supplementary Information. The simulation follows the evolution of the initial magnetization distribution over 20 ps. The pseudospectral model was solved with a Runge–Kutta 45 method (adaptive step) with renormalization of the magnetization vector at every iteration. Periodic boundary conditions inherent to Fourier transformation were used. The 2D simulation domain was 435.24 nm × 21.762 nm discretized at a cell size of 0.403 nm which was obtained as the composition-weighted average of Co and Gd lattice parameters. In addition, we used the following material parameters based on the experiments reported in ref. 9: $M_s = 250$ kA/m, Gilbert damping constant $\alpha_G = 0.02$, uniaxial anisotropy $H_k = 274$ kA/m, and $L_{ex} = 4$ nm. The resulting magnetization evolution $m_z^{(PG)}(x,y,t)$ was Fourier transformed in 2D. The TG signal was estimated as the amplitude of the Fourier peak at $\mathbf{q}$. The simulation was repeated 10 times for each C using different realizations for the noise $\xi(x, y)$ and $\eta(x, y)$, and the estimated TG signal is then averaged to minimize fluctuations. We run several sets of calculations as a function of selected values of C and L_{ex}. Qualitatively, we observe that the strength of the modulation does not only increase the amplitude of the signal but also shifts the maximum to later delays while shorter exchange lengths are responsible for longer magnetization recovery times. The case of intensity TG is described in Section 3 of the Supplementary Information.

Data availability

Processed data are available on figshare under the access code https://doi.org/10.6084/m9.figshare.27233223. Raw data are available in the open access Elettra data repository under https://doi.org/10.34965/i47529.

Code availability

The code used for the data reduction and the numerical simulations is under constant development and, therefore, is not yet released in a public repository. It is available from the corresponding author under request.

References

1. Rotenberg, N. & Kuipers, L. Mapping nanoscale light fields. *Nat. Photonics* **8**, 919–926 (2014).
2. Manjavacas, A., Zundel, L. & Sanders, S. Analysis of the limits of the near-field produced by nanoparticle arrays. *ACS Nano* **13**, 10682–10693 (2019).
3. Burresi, M. et al. Observation of polarization singularities at the nanoscale. *Phys. Rev. Lett.* **102**, 033902 (2009).
4. Zhao, R. et al. Nanoscale polarization manipulation and encryption based on dielectric metasurfaces. *Adv. Opt. Mater.* **6**, 1800490 (2018).
5. Bencivenga, F. et al. Four-wave mixing experiments with extreme ultraviolet transient gratings. *Nature* **520**, 205–208 (2015).
6. Bencivenga, F. et al. Nanoscale transient gratings excited and probed by extreme ultraviolet femtosecond pulses. *Sci. Adv.* **5**, https://doi.org/10.1126/sciadv.aaw5805 (2019).
7. Foglia, L. et al. Extreme ultraviolet transient gratings: a tool for nanoscale photoacoustics. *Photoacoustics* **29**, 100453 (2023).
8. Bencivenga, F., Capotondi, F., Foglia, L., Mincigrucci, R. & Masciovecchio, C. Extreme ultraviolet transient gratings. *Adv. Phys.: X* **8**, https://doi.org/10.1080/23746149.2023.2220363 (2023).
9. Ksenzov, D. et al. Nanoscale transient magnetization gratings created and probed by femtosecond extreme ultraviolet pulses. *Nano Lett.* **21**, 2905–2911 (2021).
10. Yao, K. et al. All-optical switching on the nanometer scale excited and probed with femtosecond extreme ultraviolet pulses. *Nano Lett.* **22**, 4452–4458 (2022).
11. Eichler, H.J., Günter, P. & Pohl, D.W. *Laser-Induced Dynamic Gratings*. *Springer Series in Optical Sciences*, Vol. 50 (Springer, Berlin, Heidelberg, 1986).
12. Terazima, M. A new method for circular dichroism detection using cross-polarized transient grating. *J. Phys. Chem.* **99**, 1834–1836 (1995).
13. Yang, L. et al. Coherent propagation of spin helices in a quantum-well confined electron gas. *Phys. Rev. Lett.* **109**, 246603 (2012).
14. Weber, C. P. et al. Observation of spin Coulomb drag in a two-dimensional electron gas. *Nature* **437**, 1330–1333 (2005).
15. Foglia, L. et al. A new framework for soft x-ray transient gratings. *J. Phys. B: At., Mol. Opt. Phys.* **57**, 145601 (2024).
16. Mincigrucci, R. et al. Advances in instrumentation for FEL-based four-wave-mixing experiments. *Nucl. Instrum. Methods Phys. Res. Sect. A* **907**, 132–148 (2018).
17. von Korff Schmising, C. et al. Generating circularly polarized radiation in the extreme ultraviolet spectral range at the free-electron laser FLASH. *Rev. Sci. Instrum.* **88**, https://doi.org/10.1063/1.4983056 (2017).
18. Allaria, E. et al. Control of the polarization of a vacuum-ultraviolet, high-gain, free-electron laser. *Phys. Rev. X* **4**, 41040 (2014).
19. Roussel, E. et al. Polarization characterization of soft X-ray radiation at FERMI FEL-2. *Photonics* **4**, https://doi.org/10.3390/photonics4020029 (2017).
20. Lutman, A. A. et al. Polarization control in an X-ray free-electron laser. *Nat. Photonics* **10**, 468–472 (2016).
21. Deng, H. et al. Polarization switching demonstration using crossed-planar undulators in a seeded free-electron laser. *Phys. Rev. ST Accel. Beams* **17**, 20704 (2014).
22. Schmidt, T. & Calvi, M. APPLE X undulator for the SwissFEL soft X-ray beamline Athos. *Synchrotron Radiat. N.* **31**, 35–40 (2018).
23. Schneidmiller, E. & Yurkov, M. V. Reverse undulator tapering for polarization control and background-free harmonic production in XFELs: results from FLASH. In *Proc. International Free Electron Laser Conference (FEL'17)*, Santa Fe, NM, USA, August 20–25, 2017, (eds Bishofberger, K., Carlsten, B. & Schaa, V. R. W.) 106–108 (JACoW, Geneva, Switzerland, 2018).
24. Li, P., Wei, T., Li, Y. & Pflueger, J. Magnetic design of an Apple-X afterburner for the SASE3 undulator of the European XFEL. *Nucl. Instrum. Methods Phys. Res. Sect. A* **870**, 103–109 (2017).
25. Yakopov, M. et al. Characterization of helical APPLE X undulators with 90 mm period for the European XFEL. *J. Phys.: Conf. Ser.* **2380**, 12019 (2022).
26. Perosa, G. et al. Femtosecond polarization shaping of free-electron laser pulses. *Phys. Rev. Lett.* **131**, 45001 (2023).
27. Sasaki, S. Analyses for a planar variably-polarizing undulator. *Nucl. Instrum. Methods Phys. Res. Sect. A* **347**, 83–86 (1994).
28. Allaria, E. et al. Highly coherent and stable pulses from the FERMI seeded free-electron laser in the extreme ultraviolet. *Nat. Photonics* **6**, 699–704 (2012).
29. MacArthur, J. P., Lutman, A. A., Krzywinski, J. & Huang, Z. Microbunch rotation and coherent undulator radiation from a kicked electron beam. *Phys. Rev. X* **8**, 41036 (2018).
30. Ferrari, E. et al. Free electron laser polarization control with interfering crossed polarized fields. *Phys. Rev. Accel. Beams* **22**, 80701 (2019).
31. Maznev, A. A. et al. Generation and detection of 50 GHz surface acoustic waves by extreme ultraviolet pulses. *Appl. Phys. Lett.* **119**, 044102 (2021).
32. Rockwell, K., Hirst, J., Ostler, T. A. & Iacocca, E. Pseudospectral Landau–Lifshitz description of magnetization dynamics. *Phys. Rev. B* **109**, 180404 (2024).
33. Radu, I. et al. Transient ferromagnetic-like state mediating ultrafast reversal of antiferromagnetically coupled spins. *Nature* **472**, 205–208 (2011).
34. Hennecke, M. et al. Ultrafast opto-magnetic effects in the extreme ultraviolet spectral range. *Commun. Phys.* **7**, 191 (2024).
35. Schaibley, J. R. et al. Valleytronics in 2D materials. *Nat. Rev. Mater.* **1**, 16055 (2016).
36. Liu, J. & Dai, X. Anomalous Hall effect, magneto-optical properties, and nonlinear optical properties of twisted graphene systems. *npj Comput. Mater.* **6**, 57 (2020).
37. Yan, B. & Felser, C. Topological materials: Weyl semimetals. *Annu. Rev. Condens. Matter Phys.* **8**, 337–354 (2017).
38. Liebman, O., Curtis, J., Petrides, I. & Narang, P. Multiphoton spectroscopy of a dynamical axion insulator. Preprint at http://arxiv.org/abs/2306.00064 (2023).
39. Ceballos, A. et al. Role of element-specific damping in ultrafast, helicity-independent, all-optical switching dynamics in amorphous (Gd,Tb)Co thin films. *Phys. Rev. B* **103**, 024438 (2021).
40. Shirakawa, K., Fukamichi, K., Aoki, K., Masumoto, T. & Kaneko, T. The Curie temperature of amorphous and crystalline Gd–Co alloys and its pressure effect. *J. Phys. F: Met. Phys.* **15**, 961 (1985).
41. Henke, B. L., Gullikson, E. M. & Davis, J. C. X-ray interactions: photoabsorption, scattering, transmission, and reflection at $e = 50–30{,}000$ eV, $z = 1–92$. *At. Data Nucl. Data Tables* **54**, 181–342 (1993).
42. Valencia, S. et al. Faraday rotation spectra at shallow core levels: 3p edges of Fe, Co, and Ni. *N. J. Phys.* **8**, 254 (2006).
43. White, R. *Quantum Theory of Magnetism*. *Springer Series in Solid-State Sciences* Vol. 32 (Springer, Berlin, Heidelberg, 2007).

44. Iacocca, E. et al. Spin-current-mediated rapid magnon localization and coalescence after ultrafast optical pumping of ferrimagnetic alloys. *Nat. Commun.* **10**, 1756 (2019).
45. Box, G. E. P. & Muller, M. E. A note on the generation of random normal deviates. *Ann. Math. Stat.* **29**, 610–611 (1958).
46. Brown, W. F. Thermal fluctuations of a single-domain particle. *Phys. Rev.* **130**, 1677–1686 (1963).
47. Ostler, T.A. et al. Ultrafast heating as a sufficient stimulus for magnetization reversal in a ferrimagnet. *Nat. Commun.* **3**, https://doi.org/10.1038/ncomms1666 (2012).

Acknowledgements

K.Y. and C.v.K.S. acknowledge financial support by the Deutsche Forschungsgemeinschaft (DFG, German Research Foundation)—Project-ID 328545488—TRR 227, project A02. E.P. acknowledges funding from the European Union's Horizon 2020 research and innovation program under the Marie Skłodowska-Curie grant agreement No. 860553. B.W. and S.B. acknowledge support from the European Research Council, Starting Grant 715452 "MAGNETIC-SPEED-LIMIT". This work was supported in part by the Italian Ministry of Foreign Affairs and International Cooperation. This work was supported by the U.S. Department of Energy, Office of Basic Energy Sciences under Award Number DE-SC0024339 (development of 2D pseudospectral Landau-Lifshitz numerical method for transient gratings).

Author contributions

F.B., C.M., and R.C. conceived the experiment. G.Per., E.A., A.B., G.D.N., L.G., G.Pen., P.R.R., F.S., and M.T. prepared and ran the FEL machine. W.D.E. and K.Y. prepared and characterized the samples. L.F., B.W., G.Per. R.M., F.A., D.D.A, D.F., N.N.K., S.L., E.P., J.S.P.-C., D.P., and F.B. performed the experiment. L.F., B.W., and F.B. analyzed the data. M.C. and E.I. developed the 2D pseudospectral Landau–Lifshitz equation and ran simulations for transient grating experiments. L.F., C.v.K.S., S.B., and F.B. interpreted the results and wrote the manuscript. All the authors contributed to revising the paper.

Competing interests

The authors declare no competing interests.

Additional information

Supplementary information The online version contains supplementary material available at https://doi.org/10.1038/s41467-024-54799-6.

Correspondence and requests for materials should be addressed to Laura Foglia.

Peer review information *Nature Communications* thanks Jiayi SUN, Chuanxiang Tang and the other, anonymous, reviewer(s) for their contribution to the peer review of this work. A peer review file is available.